Published in final edited form as:

Invest Radiol. 2019 March ; 54(3): 129–137. doi:10.1097/RLI.0000000000000524.

High-Resolution Chest CT Imaging of the Lungs: Impact of 1024 Matrix Reconstruction and Photon-Counting-Detector CT

David J. Bartlett, MD[1], **Chi Wan Koo, MD**[1], **Brian J. Bartholmai, MD**[1], **Kishore Rajendran, PhD**[1], **Jayse M. Weaver, BA**[1], **Ahmed F. Halaweish, PhD**[2], **Shuai Leng, PhD**[1], **Cynthia H. McCollough, PhD**[1], and **Joel G. Fletcher, MD**[1]

[1]Department of Radiology, Mayo Clinic, Rochester MN 55905

[2]Siemens Healthineers, Malvern, PA 19355

Abstract

Objectives: To evaluate if a high-resolution photon-counting-detector computed tomography (PCD-CT) system with a 1024 × 1024 matrix reconstruction can improve the visualization of fine structures in the lungs compared to conventional high-resolution CT (HRCT).

Materials and Methods: Twenty-two adult patients referred for clinical chest HRCT (mean CTDI $_{vol}$ 13.58 mGy) underwent additional dose-matched PCD CT (mean $CTDI_{vol}$ 13.37mGy) after written informed consent. CT images were reconstructed at a slice thickness of 1.5 mm and an image increment of 1mm with our routine HRCT reconstruction kernels (B46 and Bv49) at 512 and 1024 matrix sizes for conventional energy-integrating-detector (EID) CT scans. For PCD CT, routine B46 kernel and an additional sharp kernel (Q65, unavailable for EID) images were reconstructed at 1024 matrix size. Two thoracic radiologists compared images from EID and PCD-CT noting the highest level bronchus clearly identified in each lobe of the right lung, and rating bronchial wall conspicuity of 3rd and 4th order bronchi. Lung nodules were also compared to the B46/EID/512 images using a 5- point Likert-scale. Statistical analysis was performed using a Wilcoxon signed rank test with a $p < 0.05$ considered significant.

Results: Compared to B46/EID/512, readers detected higher order bronchi using B46/PCD/1024 and Q65/PCD/1024 images for every lung lobe ($p<0.0015$), but in only the right middle lobe for B46/EID/1024 ($p=0.007$). Readers were able to better identify bronchial walls of the 3rd and 4th order bronchi better using the Q65/PCD/1024 images (mean Likert-scores of 1.1 and 1.5), which was significantly higher compared to B46/EID/1024 or B46/PCD/1024 images (mean difference 0.8; $p<0.0001$). The Q65/PCD/1024 images had a mean nodule score of 1 ± 1.3 for Reader 1, and −0.1 (0.9) for Reader 2, with one reader having improved nodule evaluation scores for both PCD kernels ($p<0.001$), and the other reader not identifying any increased advantage over B46/EID/1024 ($p = 1.0$).

Conclusion: High resolution lung PCD CT with 1024 image matrix reconstruction increased radiologists' ability to visualize higher order bronchi and bronchial walls without compromising

Corresponding Author Info: Joel G. Fletcher, MD, 200 First Street SW, Rochester, MN 55905, USA, Phone: 507-284-47087, Fax: 507-266-3661, fletcher.joel@mayo.edu.

nodule evaluation compared to current chest CT, creating an opportunity for radiologists to better evaluate airway pathology.

Keywords

X-ray computed tomography; photon-counting detector; image reconstruction; bronchi; interstitial lung diseases; emphysema; lung nodules

Introduction

High resolution computed tomography (HRCT) is the most common cross-sectional imaging technique for evaluating interstitial lung disease (ILD). In fact, HRCT has transformed the understanding of ILD through correlation with histopathology and functional clinical testing [1]. There is wide range of diagnostic applications for HRCT including evaluation of chronic obstructive pulmonary disease (e.g., emphysema), asbestosis, airway diseases (e.g. bronchiectasis, bronchiolitis), perilymphatic diseases (e.g. lymphangitic carcinomatosis, sarcoidosis), with many other emerging applications [2–7].

Conventional HRCT systems use energy-integrating detectors (EIDs) that utilize scintillator materials that interact with X-ray photons to generate visible light. The visible light is detected by a photodiode that produces electric signals. To prevent light from spreading between individual EID detector elements, a reflective material (septa) is placed between each element, creating an area on the detector surface that does not participate in generating an electrical signal. Consequently, this dead space on the detector reduces the geometric dose-efficiency and the system spatial resolution.

Photon-counting detector CT (PCD CT) has been shown to have similar or improved image quality, higher iodine contrast-to-noise ratio, lower electronic noise, reduced beam-hardening artifacts, and improved spatial resolution compared to EID-CT systems [8–19]. Unique to the PCD-CT system, is the detectors' ability to directly produce electrical signals from incident photon events that are proportional to the detected photon energy. As a result, the PCD is able to count and bin the photons individually based on photon energy. Since x-rays are not converted to visible light photons in PCDs, the detector does not utilize inter-pixel septa, and high spatial resolution can be achieved by using smaller detector elements without losing dose efficiency [14].

Our PCD-CT system has two high-spatial-resolution scan modes namely *Sharp* and *Ultra High Resolution* (*UHR*) modes [13, 14, 19, 20]. A recent patient and phantom study of *Sharp* and *UHR* modes showed improved in-plane spatial resolution (150 microns) and noise properties compared to the standard spatial resolution imaging PCD-CT mode (*Macro mode*), and improved noise properties and image quality compared to routine EID CT [13, 21]. The *Sharp* and *UHR* modes have nearly identical modulation transfer functions (MTFs). The *Sharp* mode also permits evaluation of multispectral data when iodine is used. If multi-energy scanning was anticipated in the future (e.g., if iodinated intravenous contrast was used), UHR would have substantially more noise owing to its smaller collimation (and consequent longer scan times), precluding routine use in chest or abdominal exams.

To display the higher spatial resolution of *Sharp* mode in the PCD-CT system, smaller image voxel sizes are required, necessitating the use of a larger image matrix [1024 × 1024]). Additionally, higher-spatial-resolution reconstruction kernels that utilize the entire frequency bandwidth of the PCD system are required. The impact of these technical differences, however, can be difficult to determine, as the increased spatial resolution is accompanied by a substantial increase in image noise. Therefore, the purpose of this study was to evaluate if the *Sharp* mode on a PCD-CT system, combined with a 1024 × 1024 image matrix reconstruction and higher resolution reconstruction kernel, can improve the visualization of small pulmonary structures compared to conventional HRCT used in our clinical practice.

Materials and Methods

Patient Recruitment

This prospective study was approved by our Institutional Review Board (IRB) and all data were handled in a HIPAA-compliant manner. Inclusion criteria consisted of adult patients undergoing a clinically-indicated outpatient thoracic HRCT between September 14, 2016 and February 23, 2018. Written informed consent was obtained from all participants before commencement of each study. Patients were excluded if they were pregnant or unable to provide written informed consent. After the clinical HRCT, patients were escorted to the research PCD-CT scanner (SOMATOM CounT; Siemens Healthcare; Malvern, PA) to undergo the research CT exam on the PCD-CT system.

CT Image Acquisition and Reconstruction

All clinical HRCT exams were performed on a 128- or 192-slice EID-CT scanner (SOMATOM Definition AS+, Definition Edge, Definition Flash, or Definition Force; Siemens Healthcare) as shown in Table 1. The section of Thoracic Imaging at our institution determines acceptable chest CT protocols, and each patient's clinical protocol was selected by the supervising radiologist. Only end-inspiratory acquisitions were used for the study, even if other acquisitions (e.g. end-expiratory scans) were obtained.

The EID scans used an automatic exposure control setting of 70 (at 0.5 s) or 140 (at 0.25 s) quality reference mAs, which varied tube current in all three planes according to patient size to deliver a standard image quality. The EID CT images for 19/22 patients were reconstructed using a B46 kernel (AS+, Definition Flash, Edge) with weighted-filtered back projection (WFBP), and 3/22 patients using the Bv49 kernel (on the Force CT system) with ADMIRE. The two kernels B46 and Bv49 have identical spatial resolution. For each patient, EID CT images were obtained at 512 × 512 (clinical reference) and 1024 × 1024 matrix sizes.

The PCD-CT system is not equipped with automatic exposure control, therefore the effective mAs on the PCD CT was adjusted to match the volume CT dose index ($CTDI_{vol}$) of the EID-CT scan. Two sets of PCD-CT images were reconstructed for each patient using B46 (WFBP) and Q65 (SAFIRE, strength-4). All images were reconstructed at 1024 × 1024 matrix size. The B46 reconstruction kernel is identical between PCD-CT and EID-CT systems. The Q65 is a very sharp kernel (designed to utilize the full spatial frequency

bandwidth of the PCD-CT system so that higher spatial resolution can be displayed; not available for EID-CT systems). The manufacturer reports a 10% kernel modulation transfer function (MTF) for the Q65 kernel of 18.9 cm^{-1} compared to a 10% kernel MTF of 7.7 cm^{-1} for the B46 kernel. All images (EID-CT and PCD-CT) were reconstructed offline on a workstation equipped with image reconstruction software (ReconCT, Siemens Healthcare, Forchheim) provided by the manufacturer. The PCD-CT images, which included all the photons in the 25–140 keV energy range, were used in our study. For convenience, we use the terminology kernel/system/matrix to collectively refer to image source and reconstruction parameters. For instance, B46/PCD/1024 refers to PCD-CT image reconstructed using B46 kernel at 1024 × 1024 matrix size.

Image Analysis

For each patient case, images were loaded onto a clinical viewing workstation and displayed in a 2×2 fashion with the B46/EID/512 images (clinical reference) located in the upper left panel. The remaining B46/EID/1024, B46/PCD/1024, and Q65/PCD/1024 images were randomly assigned to the other 3 panels. Two fellowship-trained thoracic radiologists (16 and 10 years of experience), blinded to the CT acquisition and reconstruction method of the randomly assigned images, were asked to compare the randomized images to the reference B46/EID/512 images. The readers were instructed to enlarge the images to full screen for better visualization of structures and examine one lobe at a time. The radiologists were asked to assess their ability to visualize the morphologic features of the bronchi, lung nodules, ground glass densities, and any additional anatomic or pathologic findings.

Airway evaluation was performed by first noting the highest level (more peripheral) bronchus visible in each lobe of the right lung for each of the 1024 matrix reconstructions compared to the reference clinical HRCT. The right main stem bronchus was considered to be 1st order. Radiologists were instructed to look at the right lung because of the FOV limitations imposed by the limited PCD-CT detector array associated with the prototype PCD system. Subsequently, the readers evaluated the airways of both lungs, specifically focusing on the conspicuity and sharpness of the bronchial walls of the 3rd and 4th order bronchi. The bronchial walls of the 3rd and 4th order bronchi were identified on the B46/EID/512 images in the upper left panel and compared to the randomly distributed 1024 high matrix images using a 5-point Likert-scale (−2 = definitely worse, probable decreased ability to see small bronchial filling defects or bronchiectasis; −1 = definitely worse, unclear effect on potential diagnosis; 0 = about the same or unclear benefit/decrement; +1 = definitely better, unclear effect on potential diagnosis; +2 = definitely better, probable increased ability to see small bronchial filling defects or bronchiectasis). A score was only given to the randomly assigned 1024 × 1024 image matrix images since the B46/EID/512 images were used as the clinical reference.

After the airway evaluation, the readers were instructed to examine each routine matrix EID clinical exam (upper left panel) for lung nodules. Each reader was instructed to identify up to three nodules of any size or density per patient. Each nodule identified on the clinical B46/EID/512 images was compared the same nodule’s appearance on the B46/EID/1024, B46/PCD/1024, and Q65/PCD/1024 images using the aforementioned 5-point Likert-scale

(−2 = definitely worse, probable decreased ability to see ground glass or morphologic features; −1 = definitely worse, unclear effect on diagnosis; 0 = about the same or unclear benefit/decrement; +1 = definitely better, unclear effect on diagnosis; +2 = definitely better, probable increased ability to see ground glass or morphologic features). Readers were encouraged to make additional free text comments about anatomic structures or features not observed or better observed on B46/EID/512 reference images.

A non-reader radiologists measured image noise for each of the image acquisition and reconstruction methods by placing a circular region of interest in well aerated portion of the peripheral right lung. The standard deviation of this measurement was reported to represent image noise.

Statistics

The ability to visualize the highest level bronchus of each right lung lobe was compared among B46/EID/512, B46/EID/1024, B46/PCD/1024, and Q65/PCD/1024 images using the Wilcoxon signed rank test. The visualization of 3rd and 4th order bronchial walls and lung nodules were compared among the B46/EID/1024, B46/PCD/1024, and Q65/PCD/1024 images using the Wilcoxon signed rank test. The $CTDI_{vol}$ of the EID-CT and PCD-CT system and the image noise between types of images was also compared using the Wilcoxon signed rank test. Fischer's exact test was used to compare nodule evaluation scores between EID and PCD high matrix reconstructions (to account for cell sizes < 5). Statistical significance was defined as $p < 0.05$.

Results

Airway Evaluation

A total of twenty-two patients were included in this study (12 females [54%]; age range 37–79 years), and the mean $CTDI_{vol}$ for EID-CT scans was 13.58 mGy (25–75th percentile 10.95 −16.05 mGy). The mean $CTDI_{vol}$ for PCD-CT scans was 13.37mGy (25–75th percentile 10.63 – 15.45 mGy; p=0.718). One of the patients recruited in the study had a $CTDI_{vol}$ of 26.72 mGy on their clinical EID-CT scan and 26.02 mGy on the PCD-CT exam owing to larger size and appropriate adaptation of tube current by the EID system automatic exposure control (e.g., chest diameter 52 cm, BMI 52). The patients were scanned for the following clinical indications 45% (10/22) for pulmonary nodules, 18% (4/22) for malignancy, 18% (4/22) for abnormal CXR/pneumonia, 9% (2/22) for interstitial lung disease, 5% for bronchiectasis (1/22), and 5% (1/22) for hoarseness. Figure 1 shows the highest order (more peripheral) bronchus visualized for each 1024 matrix reconstruction for every right lung lobe in every patient. Compared to the clinical reference, higher order bronchi were only detected in the right lung middle lobe for the B46/EID/1024 (p=0.0066) images. However, higher order bronchi were detected in every right lung lobe for the B46/PCD/1024 (p=0.01) and Q65/PCD/1024 (p=0.0015) images. Compared to the B46/EID/1024 images, the B46/PCD/1024 images only detected more higher order bronchi in the right upper lobe (p=0.0018), whereas the Q65/PCD/1024 detected more higher order bronchi in the right upper and lower lobe (p=0.0015). Additionally, readers detected more 7th and 8th order bronchi in the Q65/PCD/1024 images in the upper and lower lobes compared to the

images from the other CT acquisition and image reconstruction methods ($p<0.0038$). The trend of improved visualization of higher order bronchi was more evident in the evaluations performed by Reader 2 than by Reader 1.

The readers examined the bronchial walls of the 3rd and 4th order bronchi in both lungs on the B46/EID/512 clinical reference images and compared their appearance to the 1024 ×1024 image matrix images, with a ranking of '0' indicating equivalence compared to the routine clinical images (Figures 2–3). The Q65/PCD/1024 images had significantly higher pooled mean score of 1.1 ± 0.9 and 1.5 ± 0.9 for 3rd and 4th order bronchial walls, signifying definitely better visualization, but with an unclear effect on the potential diagnosis compared to the B46/EID/512 clinical reference images (Figure 4). The B46/EID/1024 and B46/PCD/1024 images had similar mean scores for the 3rd and 4th order bronchial wall evaluation of 0.5 ± 0.5, 0.5 ± 0.6 and 0.5 ± 0.6, 0.5 ± 0.8, and were significantly lower than the scores for the Q65/PCD/1024 images ($p < 0.0001$).

Nodule Evaluation

Each reader identified up to three nodules of any size or density per patient in the B46/EID/512 clinical reference images and compared the appearance of these nodules to the 1024 ×1024 matrix images. Reader 1 identified and evaluated 43 nodules (6 ground glass, 1 part-solid, 36 solid) and Reader 2 identified and evaluated 13 nodules (2 calcified granulomas, 2 ground glass, 2 part-solid, 7 solid). The morphologic characteristics of the nodules are summarized in Table 2. The Q65/PCD/1024 images had a mean nodule evaluation score of 1 ± 1.3 for Reader 1, and -0.1 ± 0.9 for Reader 2, with relative comparison scores to the conventional B46/EID/512 images shown in Table 3. Reader 1 found that only 5% (2/43) nodules had nodule evaluation scores better than conventional images (B46/EID/512) when using a conventional CT system with high matrix (B46/EID/1024), but that 40% (17/43; B46/PCD/1024) and 72% (31/43; Q65/PCD/1024) had better nodule evaluation scores with a PCD system. Reader 1 found that both high matrix PCD kernels had significantly better nodule evaluation scores compared to EID high matrix images ($p<0.001$). Reader 2 had improved nodule evaluation scores in 31% (4/13) using EID high matrix, but this proportion did not increase with high matrix PCD kernels, and there was no difference in nodule evaluation scores between EID high matrix and PCD high matrix reconstructions ($p = 1.0$)).

Observations

The readers were asked to make free-text comments regarding the visualization of other features on the B46/EID/1024, B46/PCD/1024, and Q65/PCD/1024 images compared to the clinical reference (B46/EID/512) for each patient. Both readers made notable observations regarding the improved visualization of fibrosis, honeycombing, emphysema, bronchiectasis, and sharper nodule margins in the Q65/PCD/1024 images compared to the clinical reference (Figures 5–6). Additionally, both readers also commented on differences in the internal attenuation characteristics of lung nodules in Q65/PCD/1024 images compared to clinical EID images, but the import of these differences is unclear, as this data was not collected prospectively.

Image Noise Comparisons

Noise measurements (Table 4) showed that there was no significant difference in image noise between B46/EID/1024 and B46/PCD/1024 images (p=0.603). Similarly, no significant noise differences were noticed between B46/EID/512 and B46/PCD/1024 (p=0.637). However, there was a significant difference in noise when employing the high spatial Q65 kernel, with the high resolution Q65/PCD/1024 reconstruction having significantly more noise than either the B46/EID/1024 ($p < 0.0001$) or B46/PCD/1024 images ($p < 0.0001$). This increase in image noise could be attributed to the markedly higher spatial resolution of the Q65 kernel compared to the B46 kernel.

Discussion

The current study demonstrates that *Sharp* mode (150 micron spatial-resolution) on a PCD-CT scanner can subjectively improve the visualization of higher order bronchi and 3rd/4th order bronchial walls, and suggests that lung nodule conspicuity can be preserved compared to clinical reference images when the PCD-CT images are reconstructed with a large image matrix (1024 ×1024) and sharp kernel (Q65). The ability to detect higher order bronchi appeared to be related to the use of the1024 × 1024 image matrix as well as the smaller detector pixels available in the *Sharp* mode of the PCD-CT system. This is illustrated by having a statistically higher bronchi detection rate and better bronchial wall visualization using the high resolution PCD-CT kernel combined with a high matrix reconstruction. The PCD-CT system has a smaller detector pixel size than the EID-CT systems, and the *Sharp* mode used in our work employs 225 um subpixels to increase spatial resolution compared to the previously assessed *Macro* mode of this prototype CT system [22]. Because of the desire to reconstruct images that display the entire chest and this increased spatial resolution, a 1024 × 1024 image matrix is required using a larger FOV (275 mm) reconstruction. Using a smaller image matrix (512 × 512) for large FOV reconstructions would create a larger voxel size, reducing the spatial resolution that could be displayed and create pixelation and stair step artifacts [14]. For conventional EID systems, since the intrinsic resolution (collectively determined by the focal spot size, detector size and magnification) is not as high as the *Sharp* mode of the PCD-CT system, 512 × 512 matrix adequately meets the sampling requirements of the EID system, and further increasing the matrix size does not increase the spatial resolution.

The ability to perform larger FOV image reconstructions for lung HRCT is important because the entire lung anatomy can be evaluated in a single image. There are advantages to increasing the spatial resolution at a larger FOV as many lung pathologies, such as small airway and diffuse lung diseases, lung nodules, ILD, are often bilateral processes and require high resolution longitudinal studies for accurate diagnosis and multidisciplinary treatment [23–25]. Recently, a study demonstrated that HRCT with small FOV (≤ 100 mm) and 1024 × 1024 image matrix reconstructions for lung nodule evaluation improved image quality compared to conventional HRCT, reducing patient follow-up [26]. However, the strategy of using a small FOV to improve spatial resolution would be challenging to apply to patients who have diffuse lung disease or bilateral processes because multiple images would need to be reconstructed to cover the entire anatomy. Of note, the 275mm FOV used in this study is

not a limitation of the PCD-CT technology itself, but due to the prototype detector array of the PCD-CT system.

A recent study compared image quality of cadaver lung disease specimens using HRCT with large image matrices (1024× 1024 and 2048 × 2048) and large FOV (320 mm) image reconstruction and found improved image quality for lung disease compared to reconstructions with a 512 × 512 matrix, but at the cost of increased image noise[27]. However, in this prior study, the CT acquisitions had a larger $CTDI_{vol}$ (2–3 times) compared to routine clinical doses. An advantage of using our PCD-CT system is the ability to perform high resolution imaging at routine clinical dose levels. Another study using a whole-body photon-counting detector CT[28] evaluated the performance of a dedicated sharp reconstruction kernel for imaging stents. While the results demonstrated increased high-contrast spatial resolution from the sharp kernel for imaging metallic stents, the study was performed in vitro on phantoms, and did not evaluate the impact of large-FOV, large matrix reconstruction on soft tissue anatomic structures. To our knowledge, this is the first study to report the effects of a large FOV, large image matrix reconstruction for dose-efficient high-resolution lung imaging in patients using a PCD-CT system, in comparison to clinical reference involving conventional EID-CT systems.

Furthermore, these results demonstrate the importance of proper kernel selection to be able to convey the higher spatial resolution capabilities of the PCD-CT system. The Q65 kernel is specifically designed to accomplish image reconstruction with high spatial frequency available for a particular CT system being used, whereas the B46/Bv49 kernels are designed to visually enhance the edges (3D edge preserving) of anatomic structures to make the CT images look visually sharper to the reader while reducing image noise. The B46/Bv49 kernels are optimized for the EID CT systems on which they are used, and consequently operate within the limiting spatial resolution of those EID systems, which is lower than the maximum spatial resolution possible with the PCD-CT system. It is well know that there is correlation between spatial resolution and image noise: as spatial resolution is increased, the image noise will also increase. To control the increased noise incurred by the Q65 kernel, iterative reconstruction (SAFIRE) was used to reduce the noise of the PCD-CT images while maintaining the high spatial resolution offered by the PCD-CT system. This relationship was observed in the reader study results where the increased image noise in Q65 images compared to B46 images did not appear to limit the improvements in visualizing the higher order bronchi. This Q65 kernel is not available for the EID-CT systems.. Unlike the EID-CT acquisitions using 120kV tube potential, the PCD-CT scans used 140kV, with energy thresholds of 25 and 75 keV to allow simultaneous multi-energy acquisition. While the effects of improved spatial resolution assessed in this pilot are not dependent upon kV differences, we used 140 kV in the PCD arm of this study because it improves the spectral separation between acquired multi-energy data, for retrospective dual-energy processing, if clinically beneficial (e.g., if IV contrast were used). Additionally, the use of 140kV allows for reduced beam hardening artifacts in the (75 – 140) keV images from PCD-CT. Since this is a pilot study using a research PCD-CT system, the additional benefits from multi-energy information in the context of lung imaging require further investigation. Additionally, further improvements in image quality could be anticipated with the availability of flying focal spot and automatic exposure control.

Overall, there was preservation of lung nodule conspicuity in the 1024 matrix reconstruction images compared to clinical reference. The large discrepancy observed between mean lung nodule scores for the Q65/PCD/1024 images (1 ± 1.3 vs. -0.1 ± 0.9) is likely due to reader bias (e.g. difference in opinion on attenuation characteristics) and difference in the number of observations (43 vs. 13). Inherently, this is due to the subjective nature of the study, which should be addressed in the future by having additional radiologists evaluate the images to improve precision, as well as phantom studies with nodules of known composition. However, an important observation made by both of the readers not directly assessed in the Likert-scales was the appearance of sharper nodule borders with the Q65/PCD/1024 images compared to the clinical reference. This attribute is often desired clinically because such quality improves nodule size measurement accuracy and in turn affects patient management[29]. For example, per the Fleischner Society Guidelines, no follow up or optional 12 month follow up is recommended for solid nodules less than 6 mm while 6 mm nodules require more frequent surveillance[29]. Therefore, improved accuracy in nodule measurement rendered by the Q65/PCD/1024 images could potentially change patient management.

Our study has several limitations. Since this is a pilot study of a new technology and technique for lung HRCT, the generalizability of the results are limited. First, the patients recruited for this study underwent lung HRCT for various clinical indications; therefore, the image evaluation scales may not encompass all of the potential effects the PCD-CT system has on the images. Secondly, there were only relative comparisons made to each of the EID-CT and PCD-CT B46 and Q65 high matrix reconstructive images, which likely affected our ability to detect small differences in image quality between these image acquisition and reconstruction techniques. However, the goal and design of this study was pursued to detect only large differences between the current clinical reconstruction techniques and high matrix alternatives, which would provide valuable information for future study designs. In future studies, a focused clinical question evaluating the PCD-CT system's ability to help with diagnosis and clinical management of particular disease processes is necessary. For instance, the readers appreciated better visualization of fibrosis for the PCD-CT in some of the patient scans; however, we did not have enough power in our study to precisely and accurately test this comparison, thus evaluating the benefit PCD-CT in patients with diseases that cause lung fibrosis (e.g. ILD) is of great interest. The two readers evaluated different numbers of pulmonary nodules with subjectively different impressions of the relative benefit of the PCD system on nodule evaluations, and reader training and further study is needed to assess the benefit of PCD for lung nodule detection and analysis. Lastly, the sample size of this study was small. Increasing the sample size would have been beneficial and may have created a better understanding of the effect of PCD-CT on nodule visualization. However, this study was purposely designed with a smaller sample size to guide further research regarding potential clinical applications of PCD CT.

In conclusion, the PCD-CT system, coupled with a 1024 matrix reconstruction, improved the detection of higher order bronchi compared to the EID-CT system, regardless of the image reconstruction kernel used. The addition of a sharp reconstruction kernel designed to maximize the spatial resolution of the PCD-CT system (Q65) further improved the visualization of small bronchi and bronchial walls. The results of this study demonstrate the potential benefit of PCD-CT lung HRCT, particularly in assessing airway diseases. The data

also suggest that the PCD-CT system offers benefit in visualizing other pathologies, such as fibrosis, honeycombing, and emphysema, but further studies are needed to investigate these specific lung pathologies.

Acknowledgments

Conflicts of Interest and Source of Funding:

Drs. McCollough and Fletcher receive grant support to Mayo Clinic from Siemens Healthineers. Dr. Ahmed Halaweish is an employee of Siemens Healthineers. For the remaining authors none were declared. Research reported in this article was supported by the National Institutes of Health under award number BRP 016966 and C06 RR018898. The content is solely the responsibility of the authors and does not necessarily represent the official views of the National Institute of Health.

References

1. Walsh SL, Hansell DM. High-resolution CT of interstitial lung disease: a continuous evolution. Semin Respir Crit Care Med. 2014;35(1):129–44. [PubMed: 24481766]
2. Criado E, Sanchez M, Ramirez J, et al. Pulmonary sarcoidosis: typical and atypical manifestations at high-resolution CT with pathologic correlation. Radiographics. 2010;30(6):1567–86. [PubMed: 21071376]
3. Gamsu G, Salmon CJ, Warnock ML, Blanc PD. CT quantification of interstitial fibrosis in patients with asbestosis: a comparison of two methods. AJR Am J Roentgenol. 1995;164(1):63–8. [PubMed: 7998570]
4. Hackx M, Bankier AA, Gevenois PA. Chronic obstructive pulmonary disease: CT quantification of airways disease. Radiology. 2012;265(1):34–48. [PubMed: 22993219]
5. Lynch DA, Austin JH, Hogg JC, et al. CT-Definable Subtypes of Chronic Obstructive Pulmonary Disease: A Statement of the Fleischner Society. Radiology. 2015;277(1):192–205. [PubMed: 25961632]
6. Stein MG, Mayo J, Muller N, et al. Pulmonary lymphangitic spread of carcinoma: appearance on CT scans. Radiology. 1987;162(2):371–5. [PubMed: 3797649]
7. Teel GS, Engeler CE, Tashijian JH, duCret RP. Imaging of small airways disease. Radiographics. 1996;16(1):27–41. [PubMed: 10946688]
8. Gutjahr R, Halaweish AF, Yu Z, et al. Human Imaging With Photon Counting-Based Computed Tomography at Clinical Dose Levels: Contrast-to-Noise Ratio and Cadaver Studies. Invest Radiol. 2016;51(7):421–9. [PubMed: 26818529]
9. Kappler S, Glasser F, Janssen S, et al. A research prototype system for quantum-counting clinical CT. Proc SPIE Medical Imaging. 2010;7622(76221Z).
10. Kappler S, Hannemann T, Kraft E, et al. First results from a hybrid prototype CT scanner for exploring benefits of quantum-counting in clinical CT. Proc SPIE Medical Imaging. 2012;8313(83130X).
11. Kappler S, Henning A, Krauss B, et al. Multi-energy performance of a research prototype CT scanner with small-pixel counting detector. Proc SPIE Medical Imaging. 2013;8668(86680O).
12. Kappler S, Henning A, Kreisler B, et al. Photon counting CT at elevated X-ray tube currents: contrast stability, image noise and multi-energy performance. Proc SPIE Medical Imaging. 2014;9033(90331C).
13. Leng S, Rajendran K, Gong H, et al. 150-mum Spatial Resolution Using Photon-Counting Detector Computed Tomography Technology: Technical Performance and First Patient Images. Invest Radiol. 2018.
14. Leng S, Yu Z, Halaweish A, et al. Dose-efficient ultrahigh-resolution scan mode using a photon counting detector computed tomography system. J Med Imaging (Bellingham). 2016;3(4):043504. [PubMed: 28042589]
15. Pourmorteza A, Symons R, Sandfort V, et al. Abdominal Imaging with Contrast-enhanced Photon-counting CT: First Human Experience. Radiology. 2016;279(1):239–45. [PubMed: 26840654]

16. Symons R, Reich DS, Bagheri M, et al. Photon-Counting Computed Tomography for Vascular Imaging of the Head and Neck: First In Vivo Human Results. Invest Radiol. 2018;53(3):135–42. [PubMed: 28926370]
17. Yu Z, Leng S, Jorgensen SM, et al. Evaluation of conventional imaging performance in a research whole-body CT system with a photon-counting detector array. Phys Med Biol. 2016;61(4):1572–95. [PubMed: 26835839]
18. Yu Z, Leng S, Kappler S, et al. Low-dose performance of a whole-body research photon-counting CT scanner. Proc SPIE Medical Imaging. 2013;9783(97835Q).
19. Zhou W, Montoya J, Gutjahr R, et al. Lung nodule volume quantification and shape differentiation with an ultra-high resolution technique on a photon-counting detector computed tomography system. J Med Imaging (Bellingham). 2017;4(4):043502. [PubMed: 29181429]
20. Mannil M, Hickethier T, von Spiczak J, et al. Photon-Counting CT: High-Resolution Imaging of Coronary Stents. Invest Radiol. 2018;53(3):143–9. [PubMed: 28945655]
21. Symons R, Pourmorteza A, Sandfort V, et al. Feasibility of Dose-reduced Chest CT with Photon-counting Detectors: Initial Results in Humans. Radiology. 2017;285(3):980–9. [PubMed: 28753389]
22. Leng S, Gutjahr R, Ferrero AF, et al. Ultra-high spatial resolution, multi-energy CT using photon counting detector technology. Proc SPIE. 2017;10132–101320Y.
23. Bonavita J, Naidich DP. Imaging of bronchiectasis. Clin Chest Med. 2012;33(2):233–48. [PubMed: 22640843]
24. Elicker BM, Kallianos KG, Henry TS. The role of high-resolution computed tomography in the follow-up of diffuse lung disease: Number 2 in the Series “Radiology” Edited by Nicola Sverzellati and Sujal Desai. Eur Respir Rev. 2017;26(144).
25. Naidich DP, Bankier AA, MacMahon H, et al. Recommendations for the management of subsolid pulmonary nodules detected at CT: a statement from the Fleischner Society. Radiology. 2013;266(1):304–17. [PubMed: 23070270]
26. Zhu H, Zhang L, Wang Y, et al. Improved image quality and diagnostic potential using ultra-high-resolution computed tomography of the lung with small scan FOV: A prospective study. PLoS One. 2017;12(2):e0172688. [PubMed: 28231320]
27. Hata A, Yanagawa M, Honda O, et al. Effect of Matrix Size on the Image Quality of Ultra-high-resolution CT of the Lung: Comparison of 512 × 512, 1024 × 1024, and 2048 × 2048. Acad Radiol. 2018;25(7):869–76. [PubMed: 29373211]
28. von Spiczak J, Mannil M, Peters B, et al. Photon Counting Computed Tomography With Dedicated Sharp Convolution Kernels: Tapping the Potential of a New Technology for Stent Imaging. Invest Radiol. 2018;53(8):486–94. [PubMed: 29794949]
29. MacMahon H, Naidich DP, Goo JM, et al. Guidelines for Management of Incidental Pulmonary Nodules Detected on CT Images: From the Fleischner Society 2017. Radiology. 2017;284(1):228–43. [PubMed: 28240562]

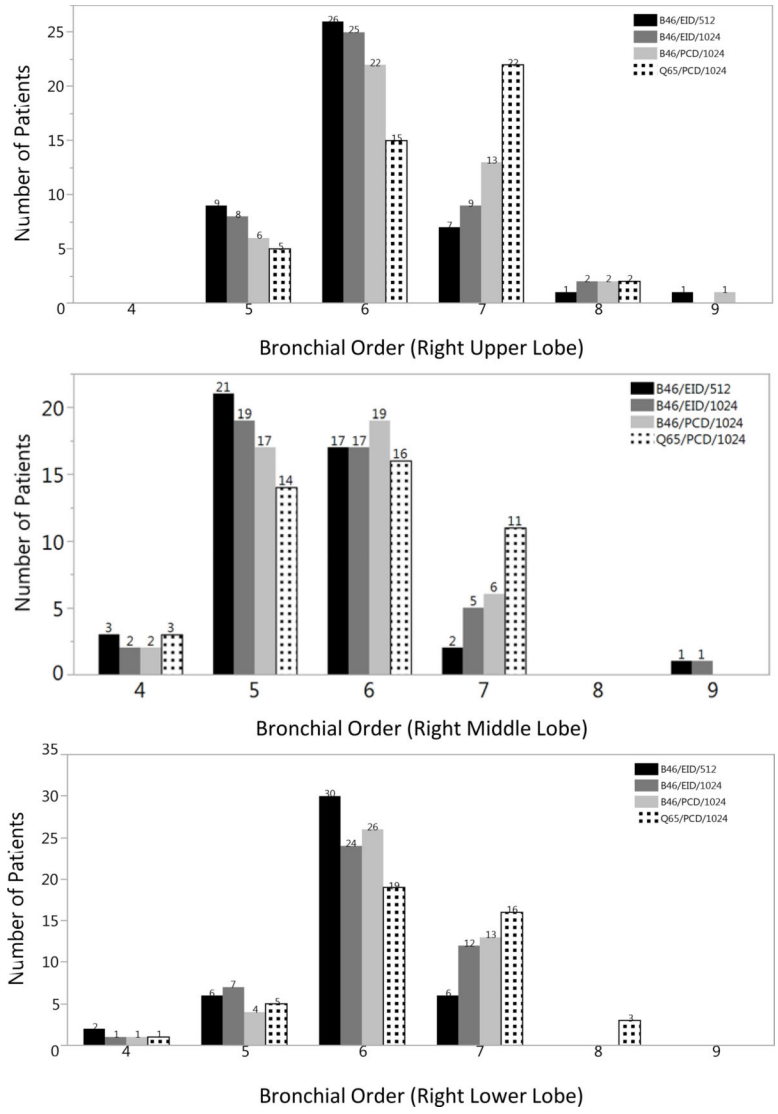

Figure 1.

Bar plots of the frequency of higher (more peripheral) bronchial order detection for both readers in right upper (a), middle (b), and lower (c) lobes by CT acquisition and image reconstruction method. Higher order bronchi were detected in all right lung lobes for the PCD-CT images with 1024 ×1024 matrices regardless of the kernel used (light grey (B46), patterned (Q65) bars) compared to clinical reference (black bar) (a-c). The addition of the Q65 sharp kernel (patterned bars) increased the detection of 7th and 8th order bronchi compared to all other CT acquisition and image reconstruction methods.

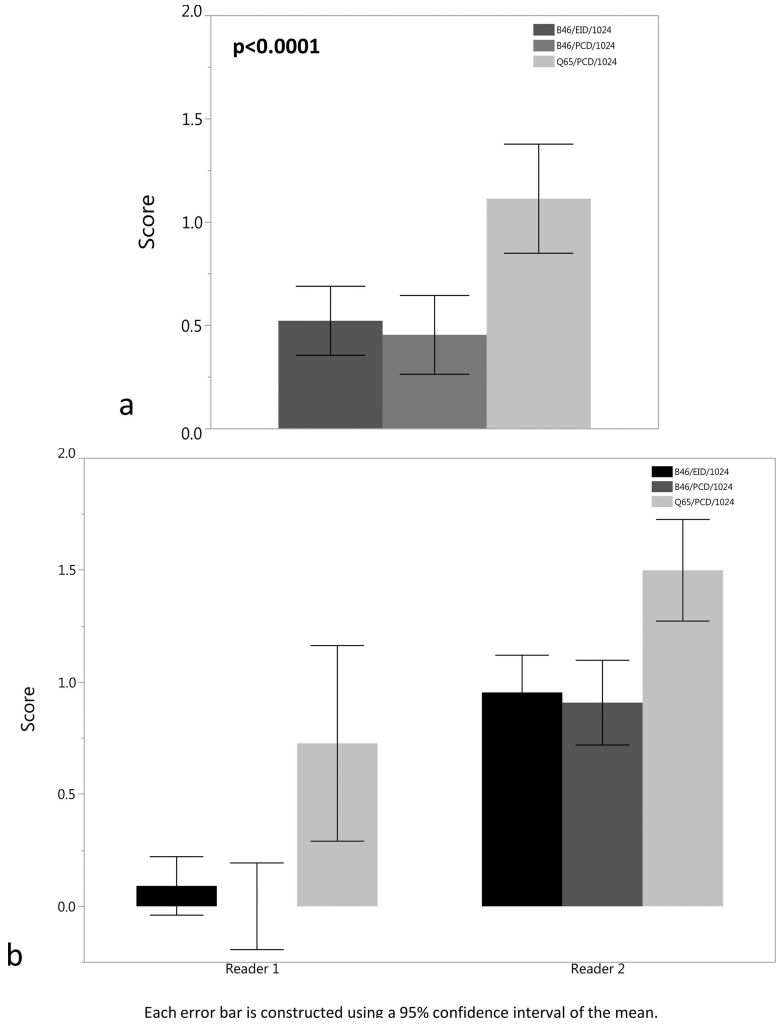

Figure 2.

(a-b). (a) Bar plot of mean score for 3rd order bronchial wall evaluation for the B46/EID/1024, B46/PCD/1024, and Q65/PCD/1024 images compared to clinical reference (B46/EID/512) images demonstrating definitely better visualization of the 3rd order bronchial walls for the Q65/PCD/1024 images (mean = 1.1). The Q65/PCD/1024 mean score is also statistically higher than the B46/EID/1024 (mean= 0.5) and B46/PCD/1024 (mean= 0.5) images (p <0.0001).**(b)** Bar plot demonstrating 3rd order bronchial wall evaluation by individual reader.

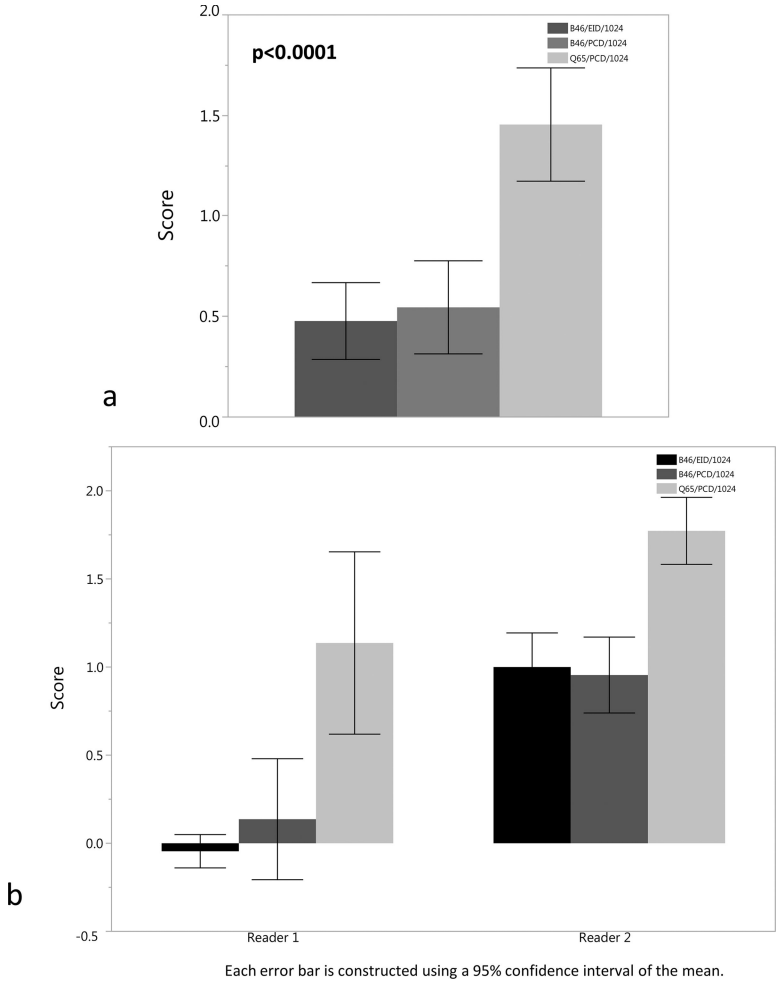

Figure 3.

(a-b). (a) Bar plot of mean score for 4th order bronchial wall evaluation for the B46/EID/1024, B46/PCD/1024, and Q65/PCD/1024 images compared to clinical reference (B46/EID/512) images demonstrating definitely better visualization of the 4th order bronchial walls for the Q65/PCD/1024 images (mean = 1.5). The Q65/PCD/1024 mean score is also statistically higher than the B46/EID/1024 (mean= 0.5) and B46/PCD/1024 (mean= 0.5) images ($p < 0.0001$). **(b)** Bar plot demonstrating 4th order bronchial wall evaluation by individual reader.

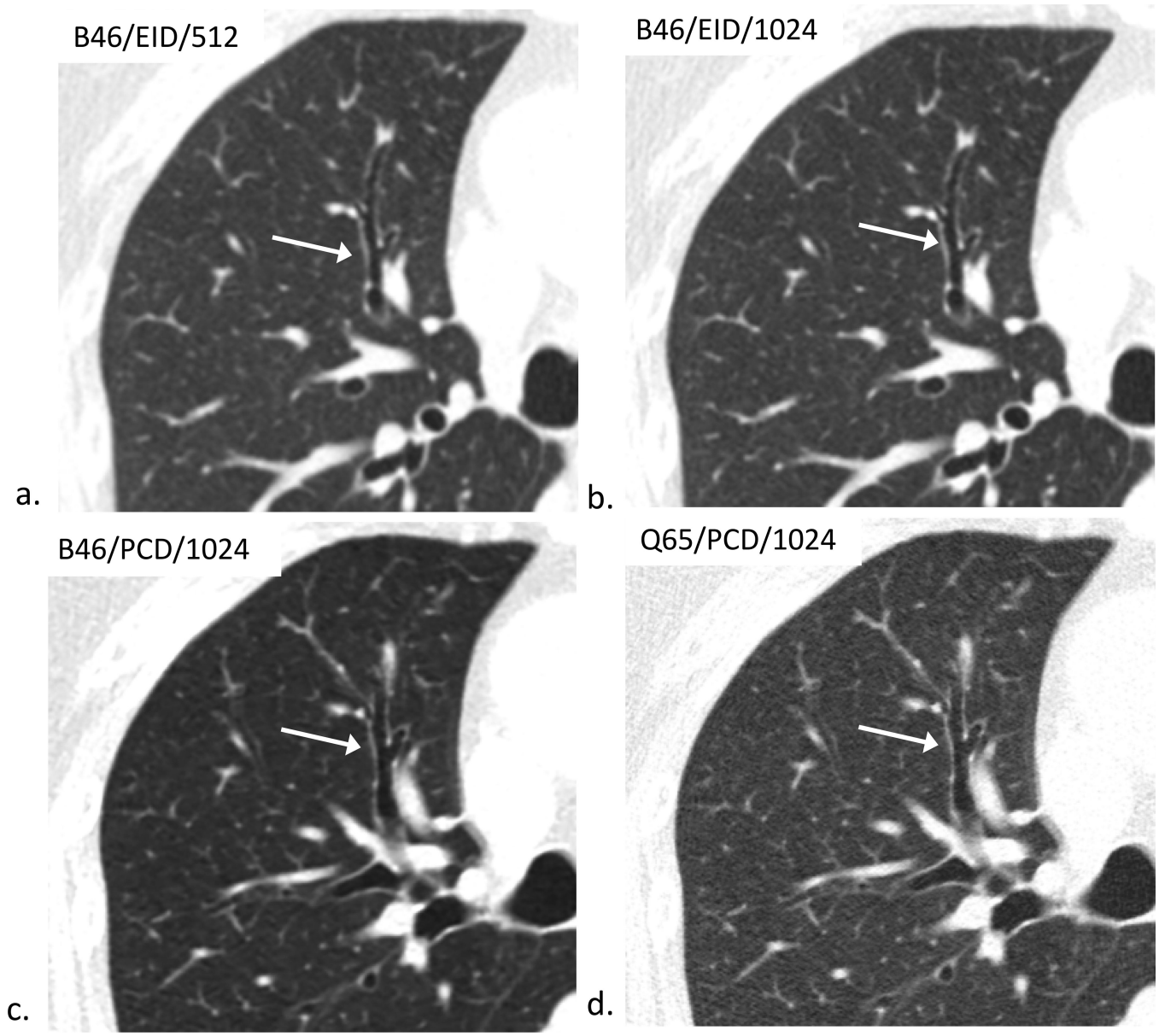

Figure 4.

80-year-old female evaluated for hemoptysis. B46/EID/512 (a), B46/EID/1024 (b), B46/PCD/1024 (c), Q65/PCD/1024 (d) images demonstrating improved visualization of the same normal 4th order bronchial wall in the Q65/PCD/1024 (d) image compared to clinical reference (a). The readers mean evaluation scores for 4th order bronchial wall evaluations were 0.5 (b), 0.5 (c), and 1.5 (d), respectively; W/L = 1200/−600 HU.

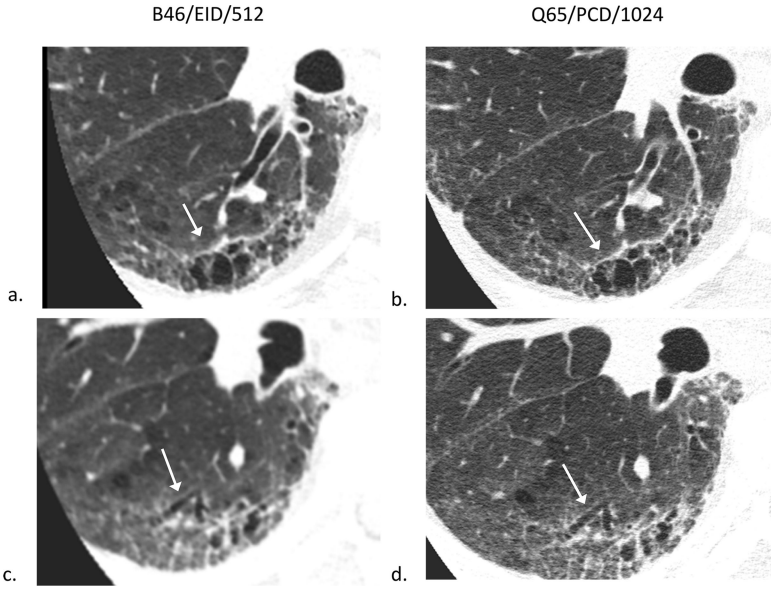

Figure 5.

68-year-old male evaluated for dyspnea secondary to pulmonary fibrosis caused by systemic scleroderma. B46/EID/512 clinical reference images (left side; a,c) and Q65/PCD/1024 images (right side; b,d) demonstrating improved visualization of honeycombing and fibrosis (a,b) as well as, traction bronchiectasis (c,d) in the Q65/PCD/1024 images (b,d) compared to the B46/EID/512 clinical reference images (c,d). W/L = 1200/−600 HU.

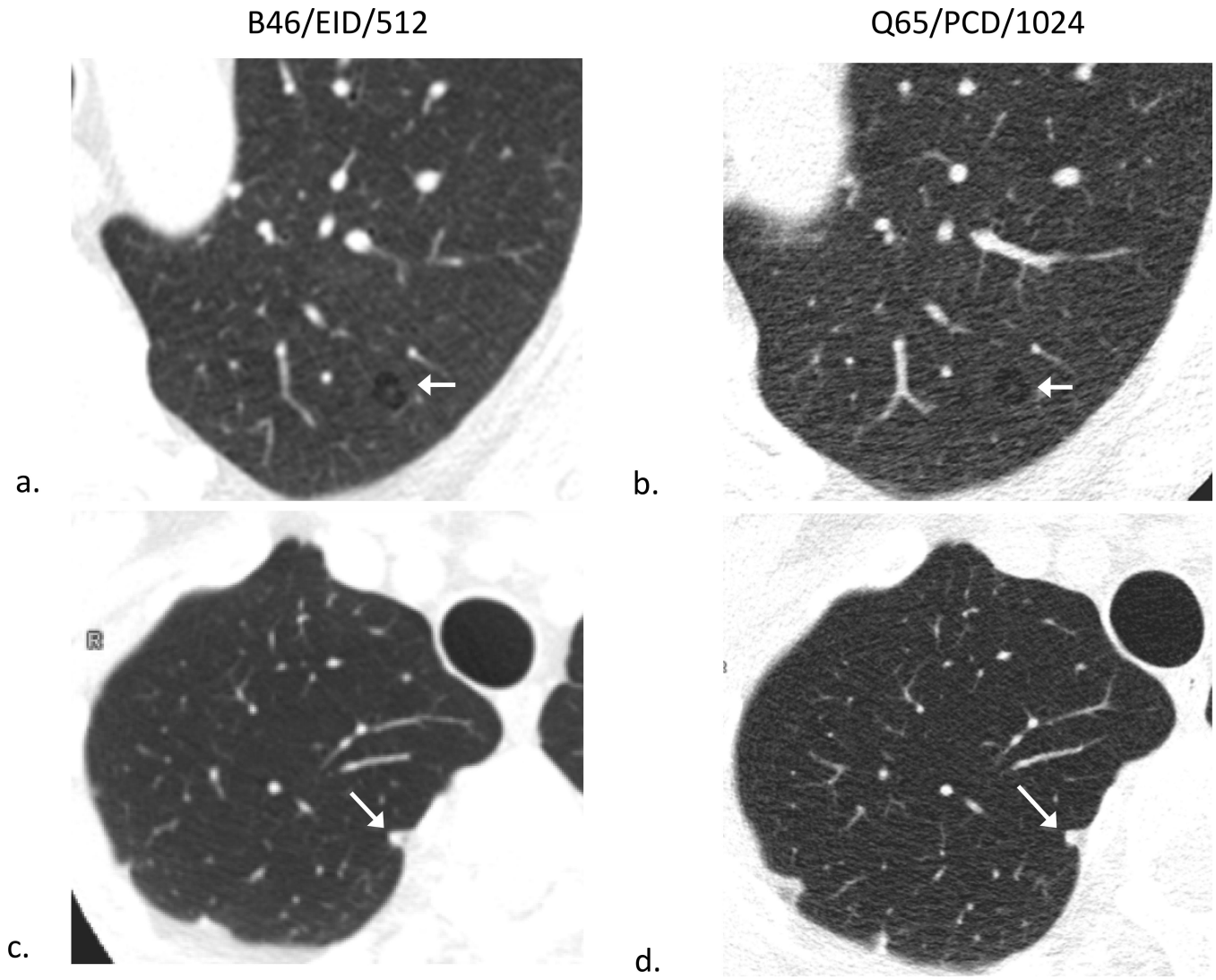

Figure 6.

B46/EID/512 (a) and Q65/PCD/1024 (b) images showing an apparent wall around a small area of centrilobular emphysema mimicking a cyst on EID images (a) and no apparent wall around the same area on PCD CT (b), compatible with emphysema. B46/EID/512 (c) and Q65/PCD/1024 (d) images of a different patient demonstrating improved visualization of margins of a 6 mm nodule on PCD CT (d) compared to EID CT (c); W/L = 1200/−600 HU.

Table 1.

Acquisition and reconstruction parameters for the conventional energy integrating detector (EID) CT system and the prototype photon counting detector (PCD) CT system in this study. (WFBP = weighted filtered back projection; ADMIRE = advanced modeled iterative reconstruction; SAFIRE = sinogram-affirmed iterative reconstruction).

CT System	**EID-CT**	**PCD-CT**
Number of patients scanned	22	
Scanner platform	Somatom Definition AS+ Somatom Definition Flash Somatom Definition Edge Somatom Definition Force	Somatom Definition CounT
Collimation	128 × 0.6 mm (AS+, Flash, Edge) 192 × 0.6 mm (Force)	48 × 0.25 mm
Rotation time	0.25s to 0.5s	0.5s
Tube potential (kV)	120	140
Quality reference mAs	70 (0.5s) or 140 (0.25s)	NA
Mean CTDIvol(32cm)	13.58 mGy (25–75th percentile 10.95–16.05)	13.37 mGy (25–75th percentile 10.63–15.45)
Energy thresholds	NA	25, 75 keV
Reconstruction technique	WFBP (AS+, Flash and Edge) ADMIRE (Force)	WFBP SAFIRE
Slice thickness/increment (mm)	1.5/1.0	1.5/1.0
Reconstruction field-of-view (mm)	275	275
Reconstruction kernel/matrix size	B46/512×512 (WFBP) B46/1024×1024 (WFBP) Bv49/512×512 (ADMIRE-Force only) Bv49/1024×1024 (ADMIRE-Force only)	B46/1024×1024 (WFBP) Q65/1024×1024 (SAFIRE)

Table 2.

Internal imaging characteristics of pulmonary nodules identified by each reader (with the reader evaluating images from both EID and PCT CT systems.

Nodule Characteristics	Calcified Granuloma	Ground Glass Opacity	Part-Solid	Solid	Mean Nodule Size mm (SD)
Reader 1 (n=43)	-	6/43 (14%)	1/43 (2%)	36/43 (84%)	5.5 (4.2)
Reader 2 (n=13)	2/13 (15%)	2/13 (15%)	2/13 (15 %)	7/13 (54%)	9.4 (7.3)

Table 3.

Reader evaluation of the morphologic features and internal characteristics of pulmonary nodules compared to conventional B46/EID/512 images using a 5-point Likert-scale (−2 = definitely worse, probable decreased ability to see ground glass or morphologic features; −1 = definitely worse, unclear effect on diagnosis; 0 = about the same or unclear benefit/decrement; +1 = definitely better, unclear effect on diagnosis; +2 = definitely better, probable increased ability to see ground glass or morphologic features; B46 and Q65 are reconstruction kernels; EID = energy integrating detector; PCD = photon counting detector; 1024 refers to high matrix reconstruction, i.e., 1024 × 1024 matrix).

Reader 1						
Imaging Strategy	**Score= −2**	**Score= −1**	**Score = 0**	**Score= 1**	**Score=2**	**Total Nodule Evaluations**
B46/EID/1024	0	2	39	2	0	43
B46/PCD/1024 *	4	2	20	14	3	43
Q65/PCD/1024 *	4	2	6	9	22	43

Reader 2						
Imaging Strategy	**Score= −2**	**Score= −1**	**Score = 0**	**Score= 1**	**Score=2**	**Total Nodule Evaluations**
B46/EID/1024	0	1	8	4	0	13
B46/PCD/1024	1	0	8	4	0	13
Q65/PCD/1024	1	2	7	3	0	13

* $p < 0.001$ compared to B46/EID/1024

Table 4.

Image noise measurements

Patient Index	EID 512 × 512 (B46 or Bv49)	EID 1024 × 1024 (B46 or Bv49)	PCD 1024 × 1024 (B46)	PCD 1024 × 1024 (Q65)
1	35	34	36	55
2	44	44	38	52
3	33	33	47	65
4	48	47	46	65
5	25	24	26	40
6	37	37	39	60
7	27	26	30	42
8	38	38	31	50
9	38	40	45	57
10*	41	40	42	80
11	34	34	42	65
12	35	34	45	61
13	45	45	50	62
14	35	35	38	63
15	42	41	53	71
16	40	39	38	58
17	58	60	51	73
18	42	46	43	73
19*	42	41	31	55
20*	39	38	38	73
21	42	42	34	58
22	40	40	32	45

*Scanned using Force (images reconstructed using Bv49 with ADMIRE)